iScience

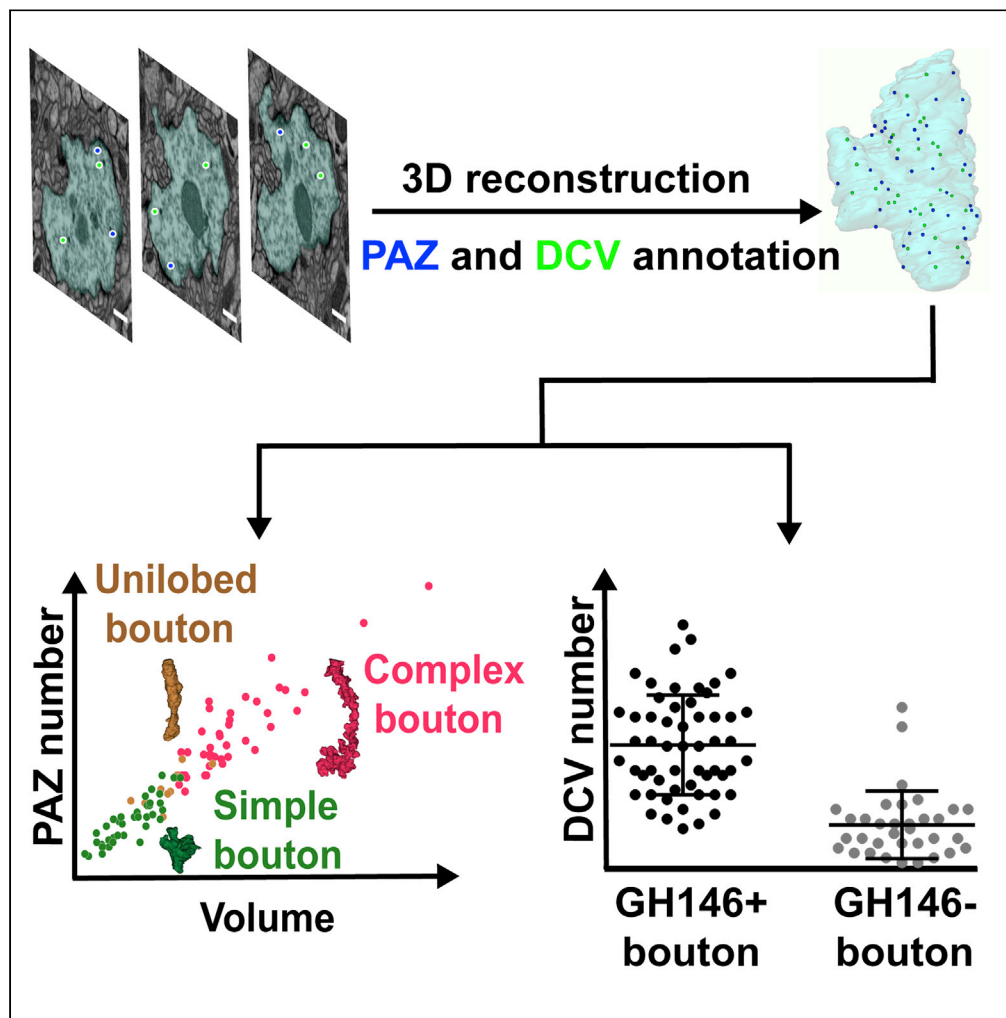**Article**

Classifying *Drosophila* olfactory projection neuron boutons by quantitative analysis of electron microscopic reconstruction

Kai Yang, Tong Liu, Ze Wang, ..., Hua Han, Zengru Di, Ke Zhang

kezhang@bnu.edu.cn

Highlights

Volumetric reconstruction categorizes neurons based on subcellular characteristics

Complex boutons contain the most presynaptic active zones and dense core vesicles

The quantity of presynaptic active zone is linearly related to the bouton size

Dense core vesicles are preferentially distributed in GH146-positive PN boutons

iScience

Article

Classifying *Drosophila* olfactory projection neuron boutons by quantitative analysis of electron microscopic reconstruction

Kai Yang,[1,2] Tong Liu,[3] Ze Wang,[3] Jing Liu,[4] Yuxinyao Shen,[5] Xinyi Pan,[5] Ruyi Wen,[5] Haotian Xie,[5] Zhaoxuan Ruan,[5] Zixiao Tan,[5] Yingying Chen,[5] Aike Guo,[3,5,6] He Liu,[3] Hua Han,[4] Zengru Di,[3] and Ke Zhang[3,7,*]

SUMMARY

In *Drosophila melanogaster*, olfactory projection neurons (PNs) convey odor information from the antenna lobe to higher brain regions. Recent transcriptomic studies reveal a large diversity of transcription factors, cell-surface molecules, neurotransmitter-coding, and neuropeptide-coding genes in PNs; however, their structural diversity remains unknown. Herein, we achieved a volumetric reconstruction of 89 PN boutons under Focused Ion Beam Scanning Electron Microscopy (FIB-SEM) and quantitatively analyzed the internal presynaptic active zones (PAZs) and dense-core vesicles (DCVs). The ultrastructure-based cluster analysis reveals three morphological distinct bouton subtypes: complex boutons, unilobed boutons, and simple boutons. The complex boutons contain the most PAZs and DCVs, which suggests that they are of the highest capability of releasing neurotransmitters and neuromodulators. By labeling a subset of boutons under FIB-SEM, we found that DCVs are preferentially distributed in certain GH146-positive subtypes. Our study demonstrates that PN boutons display distinct morphology, which may determine their capacity of releasing neurotransmitters and neuromodulators.

INTRODUCTION

In the central nervous system, neurons release neurotransmitters and neuromodulators to form functional circuits to regulate behaviors (Hyman 2005; Nusbaum and Blitz 2012; Heninger et al. 1996; Skaper 2018). How the microstructure of neural terminals supporting neurons releasing neurotransmitters or neuromodulators and resulting in shaping of the morphology of microcircuit is a critical question in the field of neuroscience. Before release, neurotransmitters are stored in small clear core vesicles that drift or dock at presynaptic active zones (PAZs), and neuromodulators are stored in large dense-core vesicles (DCVs) that drift in the cytoplasm (Gondre-Lewis et al. 2012; Kuznetsov and Kuznetsov 2017). Previous studies have shown that neuropeptides can serve as co-transmitters that modulate synaptic plasticity (Nusbaum et al. 2017; Root et al., 2011; Barnstedt et al., 2016; Hökfelt et al., 2018), suggesting that DCVs may be morphologically close to PAZs in axonal terminals. However, no direct evidence shows the spatial relationships between DCVs and PAZs and their distribution features in different subtypes of neurons. Because olfactory projection neurons (PNs) boutons display identifiable feature and contain lots of PAZs and DCVs under electron microscopy (Butcher et al., 2012), the PNs in adult fruit flies (*Drosophila melanogaster*) provide a convenient model to investigate the ultrastructure of PAZs and DCVs.

In *D. melanogaster's* olfactory circuit, PNs relay odor information from the primary olfactory center, the antenna lobe, to two brain regions, the mushroom body (MB), and the lateral horn (LH), regulating adaptive and innate behaviors, respectively (Masse et al. 2009). The calyx is the input region of the MB, where PNs transform dense-coding odor information to sparse-coding odor information in MB intrinsic Kenyon Cells (KCs) by forming a structure called the microglomerulus (Perez-Orive et al., 2002; Butcher et al., 2012; Baltruschat et al., 2021). In addition, anterior-paired lateral neurons and dopaminergic neurons innervate the microglomerulus to modulate the structure and function of PN-KC connections, which is responsible for odor coding transformation, perception, and cognition including input integration, sparse synaptic connection, and developmental plasticity (Turner et al. 2008; Li et al., 2013; Gruntman and Turner 2013;

[1]School of Basic Medicine, Guangzhou University of Chinese Medicine, Guangzhou, Guangdong 510006, China

[2]BNU-BUCM Hengqin Innovation Institute of Science and Technology, Zhuhai, Guangdong 518057, China

[3]International Academic Center of Complex Systems, Advanced Institute of Natural Sciences, Beijing Normal University at Zhuhai, Zhuhai, Guangdong 519087, China

[4]Institute of Automation, Chinese Academy of Sciences, Beijing 100190, China

[5]Huitong College, Beijing Normal University at Zhuhai, Zhuhai, Guangdong 519087, China

[6]School of Life Sciences, Shanghai University, Shanghai 200444, China

[7]Lead contact

*Correspondence: kezhang@bnu.edu.cn

https://doi.org/10.1016/j.isci.2022.104180

Elkahlah et al., 2020). The PN-KC connection network is sophisticated and is formed by many microcircuits, which are flexible and affected by growth environment and previous experience (Jortner et al. 2007; Li et al., 2020). Recent transcriptome data (Croset et al. 2018; Xie et al., 2021) and serial section electron microscopy (ssEM) results (Butcher et al., 2012) suggest that PNs release neuropeptides as a neuromodulator at their axonal boutons, as well as two types of neurotransmitters, acetylcholine and γ-aminobutyric acid (Yasuyama et al. 2002; Liang et al., 2013). Neuropeptides are stored in DCVs, and neurotransmitters are released via PAZs in PNs. However, no direct evidence showed the structural relationship of these two components.

Herein, by expressing membrane-target Horseradish Peroxidase to label a subset of PNs and volumetrically reconstructed 89 PN boutons in a reference region in the MB calyx under Focused Ion Beam Scanning Electron Microscopy (FIB-SEM), we quantitatively analyzed the internal neurotransmitter release site, PAZs, and the neuromodulator container, DCVs. We demonstrate that: (1) based on ultrastructural morphological parameters, these PN boutons can be classified into three subtypes, namely, complex bouton, unilobed bouton, and simple bouton; (2) PAZ number is linearly correlated with bouton volume, whereas there is no strong correlation between DCV number and bouton volume; (3) most DCVs are adjacent to non-synaptic membrane but not PAZs; (4) GH-146-positive PNs (HRP positive) have significantly larger numbers of DCVs than others. In summary, the study analyzed the distribution features of PAZs and DCVs in morphologically distinct PN boutons and shed light on neuromodulator function in olfactory information processing and plasticity in *D. melanogaster*.

RESULTS

PN bouton volumetric reconstruction in a reference region of the MB calyx

PNs connect to MB in the calyx region to process olfactory information (Figure 1A). The calyx exhibits a round shape from a posterior view under EM, and it is surrounded by KC cell bodies and PN processes (Figure 1B). In the MB calyx, a microglomerulus contains large presynaptic PN axonal boutons, tiny postsynaptic dendritic claws, and some other MB extrinsic neurons (Yasuyama et al., 2002; Baltruschat et al., 2021). FIB-SEM was used to collect a serial EM dataset in a volume of 20 × 20 × 25 μm in the center of the MB calyx to quantitatively analyze the properties of PN axonal boutons. The resolution in the x–y axis was 5 nm, and the resolution in the z axis was 40 nm (Figure 1C, see STAR Methods).

PN boutons were identified in individual EM sections by four distinct features: large section area, enriched clear core vesicles, PAZs, and large internal mitochondria (Yasuyama et al., 2002; Butcher et al., 2012). The center of the same PN bouton was manually connected in consecutive sections to draw the skeleton (Figure 1D1). The skeleton demonstrates the major axis and branches of a bouton. Next, PN boutons were modeled using volumetric reconstruction in 3D to depict their individual shapes. Based on the shapes, the three-dimensional features of each bouton such as volume and surface area were calculated (Figure 1D2). Under EM, most PAZs in insects such as *Drosophila* and locusts exhibit an electron-dense ribbon called a T-bar, and DCVs are large electron-dense dots (Wichmann and Sigrist 2010; Gondre-Lewis et al., 2012). Accordingly, all PAZs and DCVs in PN boutons were annotated (Figures 1D1 and 1D3). To increase the accuracy of quantitative analysis of PAZs and DCVs, PN boutons that partially extended out of the EM dataset were not reconstructed (Figure S1A). Vesicles, mitochondria, and synapses are enriched in PN boutons, whereas they are rare in PN fibers (Figure S1B). It suggests that PN fibers may be involved in signal propagation within the neuron but not communication between neurons. Therefore, we focused on PN boutons, and PN fibers were not reconstructed. In total, 89 PN boutons were reconstructed from one FIB-SEM dataset. They were uniformly distributed in the EM dataset and exhibited variable sizes and shapes. Most PN boutons were parallel with the z axis of the dataset (Figure 1E). Following the standards before, we additionally reconstructed 15 PN boutons in female adult fly brain of a previously published transmission electron microscopy camera array 2 (TEMCA2) dataset to test whether our findings are in line with the general principles among individuals ((Zheng et al., 2018; Bates et al., 2020), Figures S1C and S1D).

Classification of PN boutons based on EM volume parameters

To investigate the distributions of DCVs and PAZs in PN boutons, we first examined the features and types of these PN boutons. Several morphological parameters of the reconstructed PN boutons were analyzed by areatree and arealist function in Fiji-TrakEM2, and a PN bouton skeleton was generated. The skeleton provides several two-dimensional morphological features such as segment number and the total length of
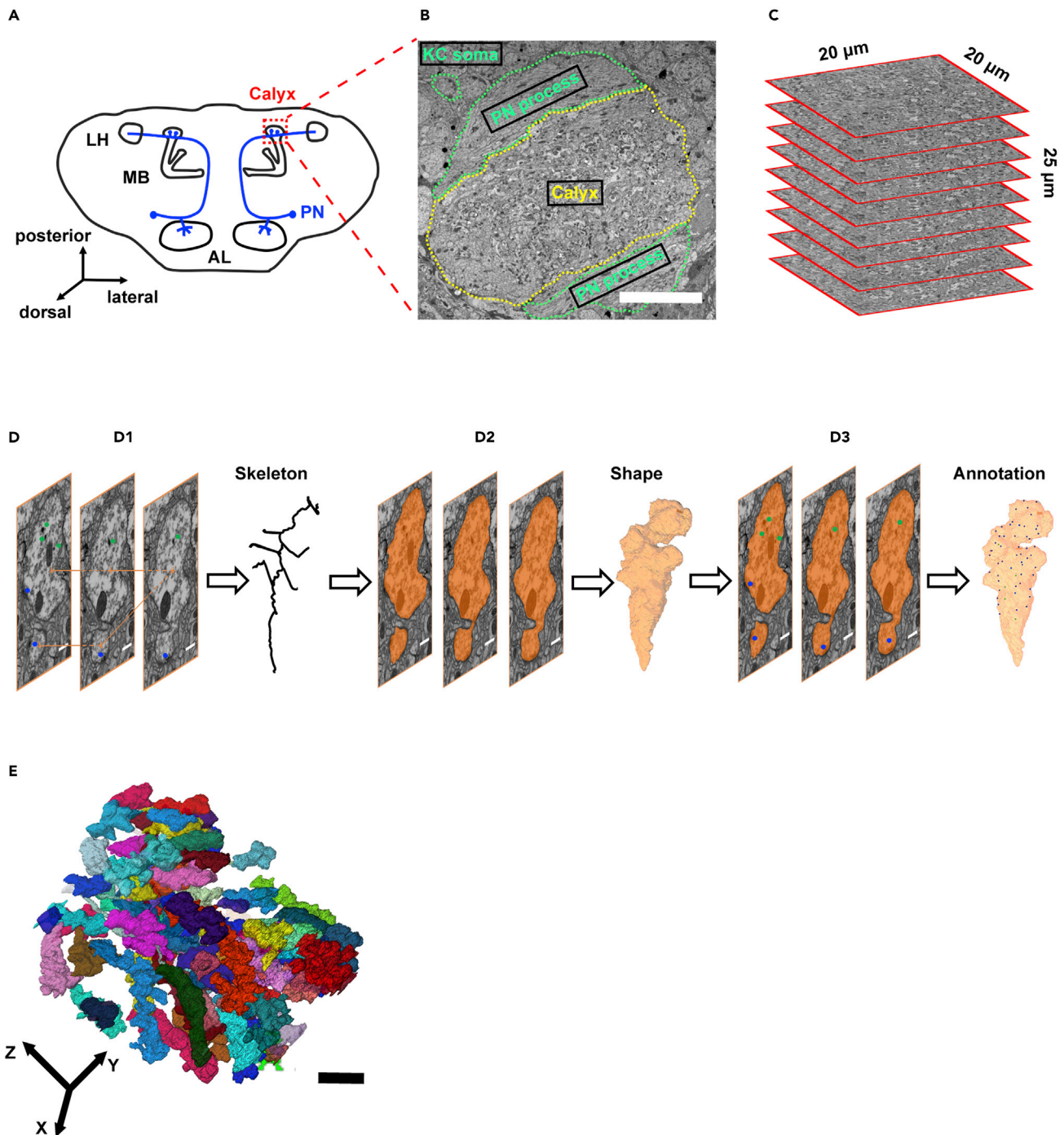
Figure 1. Volumetric reconstruction of projection neuron boutons in a reference region of the mushroom body calyx

(A) Schematic of olfactory projection neurons (PNs) in *Drosophila*. PNs connect the antenna lobe (AL) to the mushroom body (MB) and lateral horn (LH). The calyx is the input region of the MB.

(B) Posterior view of the calyx under Focused Ion Beam Scanning Electron Microscopy (FIB-SEM). PN processes and the soma of MB Kenyon cell (KC) are circled by green dotted lines, and the calyx of the MB is circled by yellow dotted lines. Scale bar = 10 μm.

(C) Raw images from FIB-SEM in the center of the calyx in a volume of 20 × 20 × 25 μm.

(D) Workflow of volumetric reconstruction of PN axonal boutons. A PN bouton was identified on individual sections and the centers of consecutive sections were connected to generate its skeleton (D1). Sections of one PN bouton were filled with the identical color to depict its shape (D2). Presynaptic active zones (PAZs, blue dots) and dense core vesicles (DCVs, green dots) were annotated in every bouton (D1 and D3). Scale bars = 5 μm.

(E) Overall view of EM-reconstructed PN boutons. 89 reconstructed PN boutons were filled with different colors. Scale bars = 5 μm.
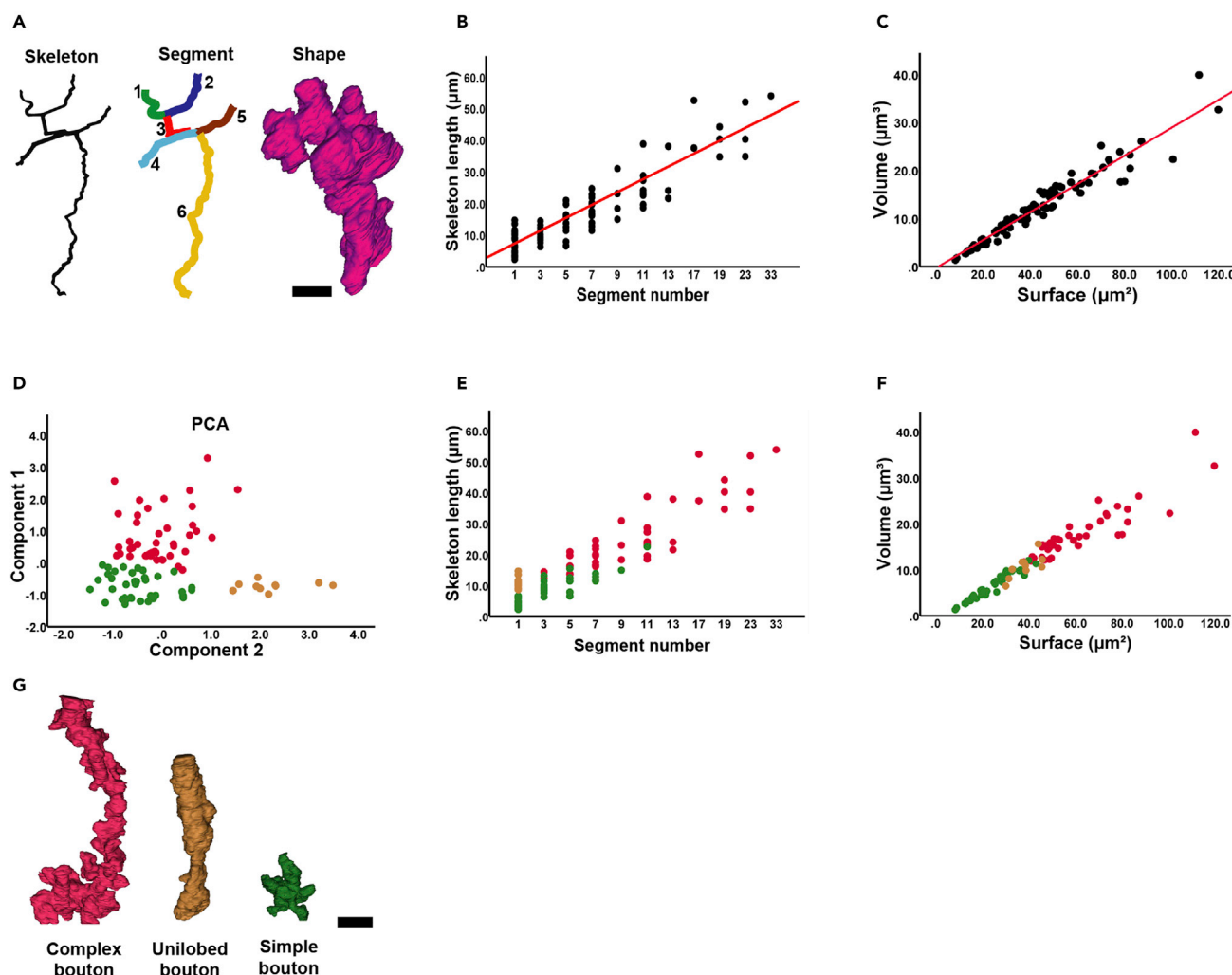
Figure 2. Morphological characteristics and classification of PN boutons

(A) Illustration of skeleton, segment, and shape. Scale bar = 5 μm.

(B) Skeleton length is positively correlated with segment number (linear line Y = 0.49X-1.60, R^2 = 0.84).

(C) Bouton volume and surface area are positively correlated (linear line Y = 0.29X-0.37, R^2 = 0.93).

(D) Two-step cluster results based on principal component analysis (PCA) of skeleton length, segment number, surface, and volume. Three subtypes were clustered and labeled by red, green, and brown. Component 1 occupied 77% of the explained variabilities and Component 2 occupied 22% of the explained variabilities.

(E) Relationship between skeleton length and segment number in different subtypes of PN boutons (red, green, and brown).

(F) Relationships between volume and surface area in different subtypes of PN boutons (red, green, and brown).

(G) Schematic of three subtypes of PN boutons. Scale bar = 5 μm.

the skeleton (Figure 2A). PN boutons contained 1 to 33 segments with a mean of approximately 7 (Table S1 and Figure S2A). The total length of PN bouton skeletons ranged from 2.3 μm to 53.9 μm, and the mean was 16.9 μm (Table S1 and Figure S2B). Total skeleton length was positively associated with the segment number (Figures 2B and S3A), indicating that each segment has a similar length, and long PNs contain a large number of segments.

The volume and surface area of PN boutons were then calculated to analyze three-dimensional features (Figure 2A). The surface area of most PN boutons was between 8.4 μm² and 119.5 μm² (mean 43.5 μm²), the volume of PN boutons ranged from 1.3 μm³ to 39.9 μm³ with a mean of 12.35 μm³, and 72/89 (80%) were between 10 μm³ and 30 μm³ (Table S1, Figures S2C and S2D). PN volume and surface area were positively correlated (Figures 2C and S3B), indicating that the surface area to volume ratio of PN boutons is
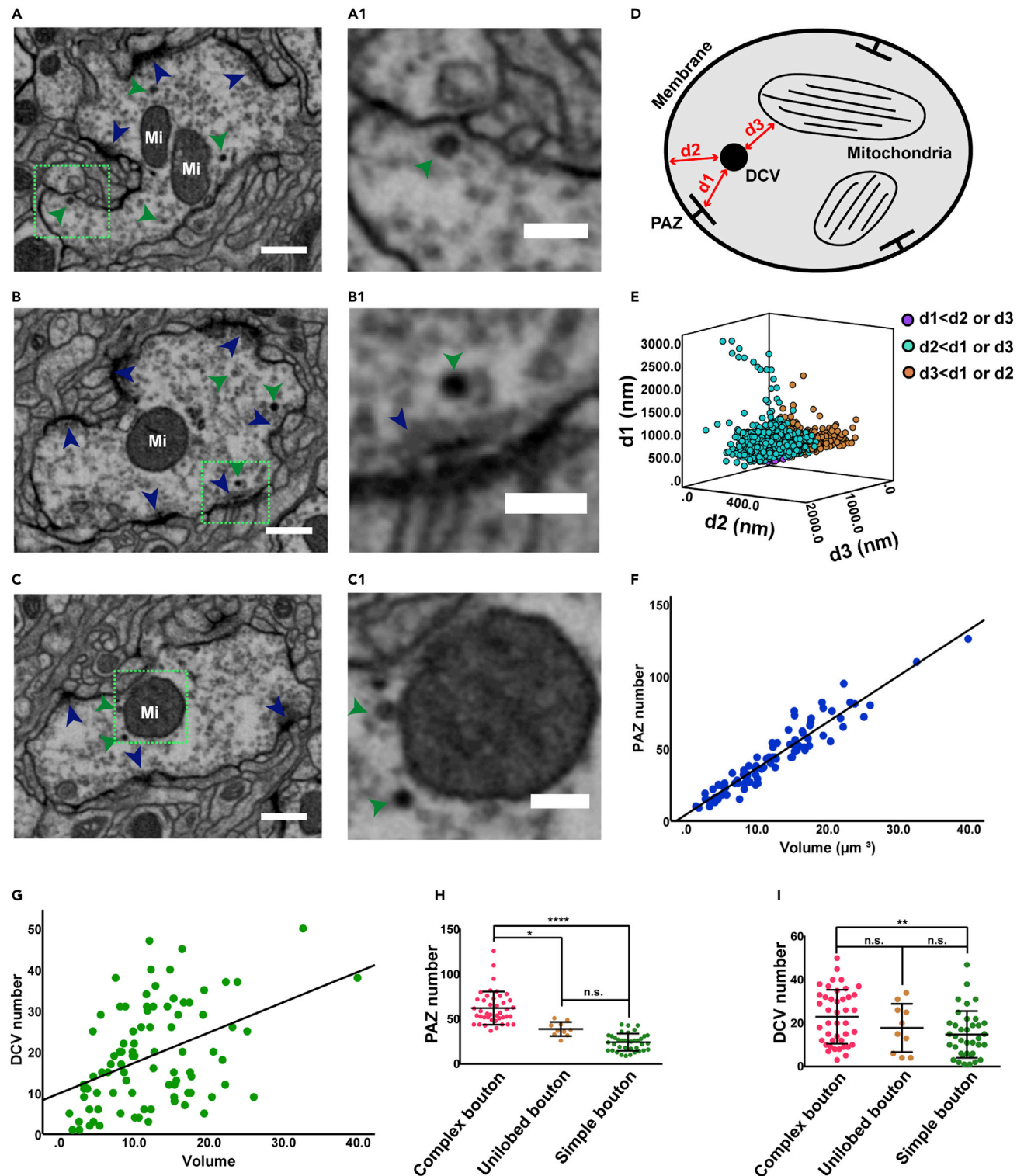
Figure 3. Subcellular distributions of PAZs and DCVs in PN boutons

(A–C) Subcellular distributions of PAZs (blue arrows) and DCVs (green arrows) in PN boutons. A1-C1 are magnified photographs of green dotted frames in A-C. Most PAZs display a feature of a T-bar ribbon (A and B), but a small number.

of PAZs have a non-ribbon structure (C). DCVs that are adjacent to membrane (A1), PAZs (B1), and mitochondria, C1). For A, B, and C, Scale bar = 500 nm. For A1, B1, and C1, Scale bar = 200 nm.

Figure 3. *Continued*

(D) Schematic of the distance from a DCV to its nearest membrane (d1), PAZ (d2), and mitochondria (d3).

(E) Scatterplots of 3 distances of all DCVs. 72.2% DCVs are near to membrane (d2<d1 or d3, cyan), 0.5% DCVs are near to PAZ (d1<d2 or d3, purple), and 27.3% DCVs are near to mitochondria (d3<d1 or d2, brown).

(F) PAZ number had a strong linear relation to bouton volume (linear line Y = 3.16X+4.74, R^2 = 0.91).

(G) DCV number was not linearly related to bouton surface area (linear line Y = 0.73X+9.93, R^2 = 0.17). (H) Complex boutons had more PAZs than unilobed boutons and simple boutons.

(I) DCV number in complex boutons was similar to that in unilobed boutons and larger than that in simple boutons. Unpaired Mann–Whitney *U* test. *p < 0.05, **p < 0.01, ****p < 0.0001, n.s. = not significant.

similar regardless of their size. Considering that the surface area to volume ratio is related to the radius of PN boutons, and the average segment length (skeleton length divided by segment number) is similar among PN boutons, these results infer that there are some intrinsic mechanisms controlling the enlargement of PN boutons.

Previous studies defined three types of PN boutons based on features determined via light microscopy (unilobed, clustered, and elongated) and two types based on features determined via electron microscopy (short segments and long slender axons) (Butcher et al., 2012). After determining all the aforementioned morphological parameters, namely, skeleton length, segment number, volume, and surface area, we performed principal component analysis (PCA) of these four parameters, and two major components were extracted (Figure 2D). Component 1 occupied 77% of the explained variabilities and Component 2 occupied 22% of the explained variabilities. Then PN boutons were automatically clustered into 3 groups via Akaike information criterion-based two-step clustering, according to component 1 and 2 from PCA analysis (Figures 2D–2G). 42 PN boutons exhibited long skeleton length, large segment number, surface area, and volume. We classified them as complex boutons. 10 PN boutons exhibited just one segment with a relatively long skeleton, and we classified them as unilobed boutons. 37 PN boutons exhibited short skeleton length, small segment number, volume, and surface area. We classified them as simple boutons (Figures 2E–2G and S4). Accordingly, PN boutons in TMECA2 dataset (Zheng et al., 2018) were also classified into 3 subtypes including 8 complex boutons, 4 simple boutons, and 3 unilobed boutons (Figure S4).

Subcellular distribution of PAZs and DCVs in PN boutons

In the central nervous system of *Drosophila*, most PAZs exhibit electron-dense ribbon T-bars, but some are non-ribbon type and are attached by an adjacent postsynaptic density (Figures 3A–3C). The neuromodulator-containing DCVs exhibit an electron-denser and larger sized ultrastructure than transmitter-contained clear core vesicles (Figures 3A–3C). Following the distinct criteria of PAZs and DCVs, we annotated all PAZs and DCVs in the volumetrically reconstructed 89 PN boutons. It is worth mentioning that with a z-step size of 40 nm during the FIB-SEM image acquisition, several PAZs and DCVs could be missed and therefore the number might be even underestimated. At subcellular level, we analyzed the distance between individual DCV with the nearest PAZ (d1), nearest membrane (d2), and the nearest mitochondria (d3) (Figure 3D, see STAR Methods). Comparing these three distances, we defined the nearest region to DCV. We analyzed 1622 DCVs in total and found that 72.2% (1171) of DCVs are near to non-PAZ membrane (d2<d1 or d3, Figures 3A1 and 3E), 0.5% (8) of DCVs are close to PAZ (d1<d2 or d3, Figures 3B1, and 3E), and 27.3% (443) of DCVs are located to mitochondria (d3<d1 or d2, Figures 3C1 and 3E). These analyses of distances demonstrate that major DCVs are close to the non-synaptic site of the membrane. It suggests that neuromodulators are likely released through non-synaptic paths (Van Bockstaele, Colago and Valentino 1996; Torrealba and Carrasco 2004). 27.3% DCVs that near to mitochondria may result from that some mitochondria-produced hydrogen peroxide functions as signaling cue to neuropeptide releasing (Jia and Sieburth 2021), or both mitochondria and DCVs are transported through microtubules to axonal terminals (Gondre-Lewis et al., 2012; Mandal et al., 2021).

PAZ number and DCV number are variable among PN boutons. PN boutons contained approximately 19 DCVs on average, with a maximum of 49 and a minimum of 1 (Table S1 and Figure S2E). Moreover, approximately 44 PAZs per PN bouton were detected on an average, with a maximum of 126 and a minimum of 9 (Table S1 and Figure S2F). To investigate the PAZ and DCV distributions in different subtypes of PN boutons, we analyzed correlations between PAZ number, DCV number, and volume in PN boutons. PAZ number was positively associated with bouton volume, and DCV number was weakly associated with bouton volume (Figures 3F, 3G, S3C, and S3D). These results indicate that PAZs are uniformly distributed in boutons, and DCV distribution is weakly associated with the morphology of PN boutons. PAZ and DCV

distributions in three PN bouton subtypes were investigated. There were significantly more PAZs in complex boutons than in unilobed boutons and simple boutons, which is consistent with the volume difference among them (Figures 2F and 3H); however, there were significantly more DCVs in complex boutons than in simple boutons, but the numbers of DCVs were similar in complex boutons and unilobed boutons (Figure 3I).

DCVs are enriched in GH146-positive boutons

To investigate the relationship between PAZ and DCV distributions, all of the reconstructed PN boutons were categorized into four clusters based on PAZ and DCV numbers via a Bayesian information criterion-based two-step clustering method (Figure 4A). PAZ and DCV numbers in different groups were compared to confirm the classifications (Figures 4B and 4C). Fewer boutons contained large numbers of both PAZs and DCVs, compared to other subtypes (Figure 4D). RNA-seq investigations indicated that PN subtypes labeled with abnormal chemosensory jump 6 (acj6) strongly expressed the sNPF gene, and PN subtypes labeled with ventral veins lacking (vvl) expressed the neuropeptide tachykinin gene (Croset et al., 2018). The two gene markers, acj6 and vvl, were exclusively expressed in anterodorsal PNs and lateral PNs that were labeled with GH146-GAL4 (Li et al., 2017; Lai et al., 2008). We then tested the hypothesis that the distribution of DCVs and PAZs are associated with genetically different PN subtypes. To determine the DCV distribution in GH146-positive and GH146-negative PNs, GH146-positive boutons were labeled using UAS-mCD8:HRP, which is driven by GH146-GAL4. The membranes of GH146-positive boutons were electron- denser than those of GH146-negative boutons as determined via EM (Schikorski et al. 2007) (Figures 4E and 4F). More than half of GH146-positive PN boutons were in clusters 1 and 2, whereas most GH146-negative boutons were in clusters 3 and 4 (Figures 4G and 4H). These results indicate that GH146-positive PNs release neuromodulators, besides neurotransmitters, but GH146-negative PNs may only release neurotransmitters to process olfactory information.

DISCUSSION

In the current study, we volumetrically reconstructed 89 PN boutons in a reference region of the MB calyx in adult *D. melanogaster* and revealed some distribution features of the neurotransmitter releasing sites, PAZs and neuropeptide-container, DCVs. Morphological parameter-based cluster analysis indicated three different subtypes of PN boutons in the calyx, including long and multiple-branched complex boutons, unilobed boutons with one long branch, and simple boutons with a few branches. At the subcellular level, we found that most DCVs are adjacent to the membranes, instead of the PAZs. PAZs are uniformly distributed on the surface of all boutons at a density of 1 PAZ per square micron. GH146-positive boutons contained significantly more DCVs than other boutons. It indicates that GH146-positive PNs release both neurotransmitters and neuromodulators, whereas other PNs mainly release neurotransmitters. This study demonstrates the quantitative distributions of PAZs and DCVs in different PN subtypes, which will shed light on neural modulation in the microcircuit of the fly olfactory system.

Morphological categorization of PN boutons

Olfactory PNs convey odor information from the antenna lobe to the MB and form microglomeruli in calyx. In the microglomerulus, large PN boutons are surrounded by distinct tiny Kenyon cell claws and other MB extrinsic neuropils, such as anterior-paired lateral neurons and dopaminergic neurons (Leiss et al., 2009; Liu and Davis 2009; Mao and Davis 2009). Previous studies have shown that PN boutons in the MB calyx are distributed in a stereotypic pattern and exhibit no subregion preference (Lin et al., 2007). Connections in the microglomerulus are the basis of divergent features for olfactory information transmission and modulation by external neurons (Scheffer et al., 2020; Li et al., 2020; Baltruschat et al., 2021). Under light microscopy, it is reported that PN boutons exhibit three patterns: unilobed, elongated, and clustered (Butcher et al., 2012). In the present study, by volumetric reconstruction, PN boutons are classified into three subtypes based on their ultrastructural features. Complex boutons exhibit large size and segment number (Butcher et al., 2012) (Figures 2E-2G); therefore, the complex boutons correspond to clustered boutons. The unilobed boutons that we identified had one long skeleton without branches (Figures 2E and 2G); therefore, they are morphologically similar to elongated boutons under light microscopy. Unilobed boutons under light microscopy with short skeleton and small branches correspond to simple boutons under EM. Axons undergo remodeling during development and in mature brains, including axon branching and pruning (Butz et al. 2009; Jamann et al. 2018; De Paola et al., 2006). Thus, these three subtypes of boutons
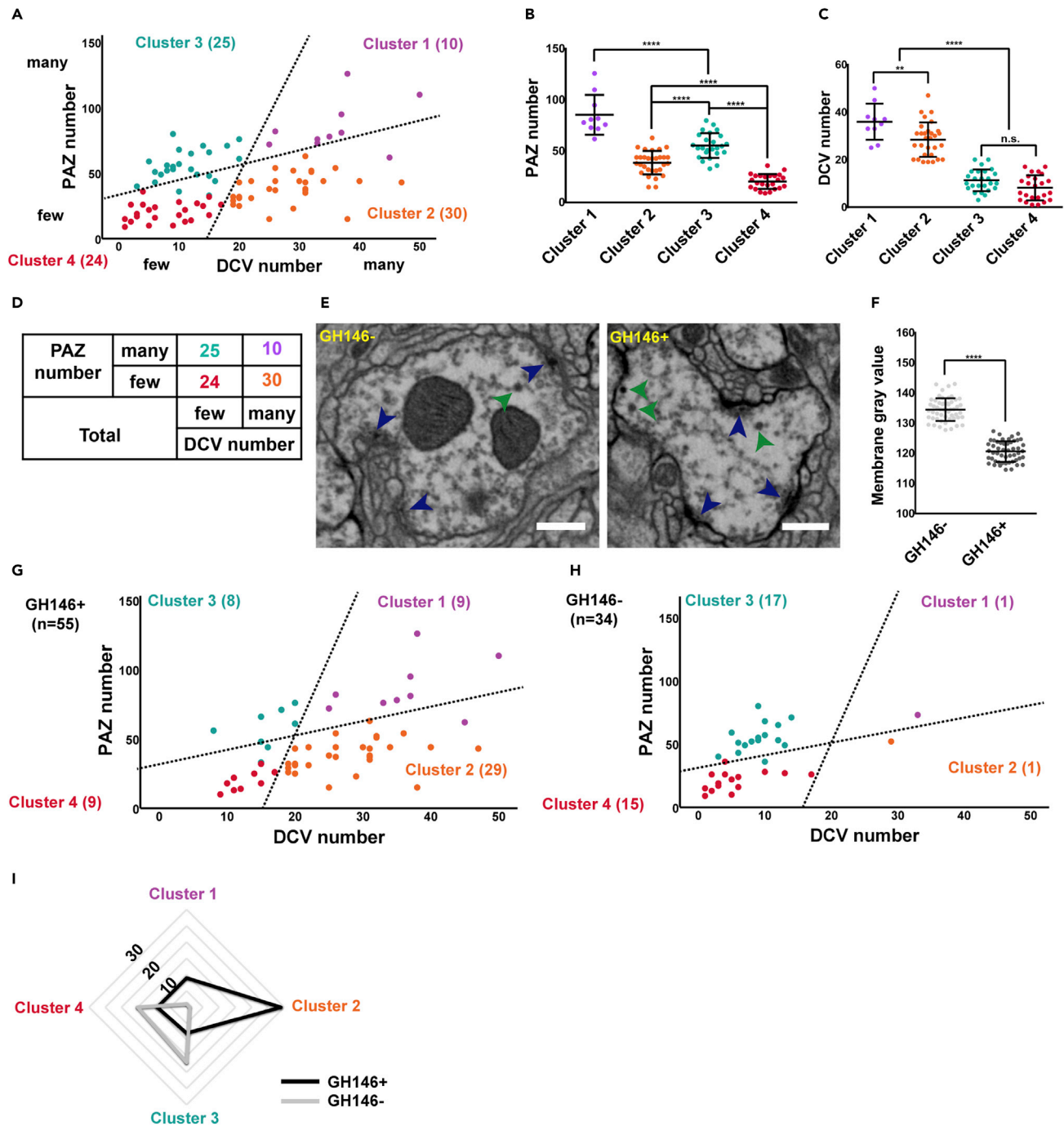
Figure 4. DCVs are enriched in GH146-positive PN boutons

(A) Clustering analysis based on PAZ number and DCV number in individual PN boutons. Four clusters are evident: boutons containing many PAZs and many DCVs (violet), boutons containing many PAZs and few DCVs (cyan), boutons containing few PAZs and many DCVs (orange), and boutons containing few PAZs and few DCVs (red).

(B and C) PAZ and DCV number comparisons in different clusters (Unpaired Mann–Whitney U test. **$p < 0.01$, ****$p < 0.0001$, n.s. = not significant).

(D) Bouton numbers in each cluster.

(E) PAZs and DCVs in GH146-negative (GH146-) and GH146-positive (GH146+) boutons. Green arrows indicate DCVs, and blue arrows indicate PAZs. Scale bar = 5 μm.

(F) Membrane gray value in GH146-positive membranes was significantly lower than that in GH146-negative membranes (Unpaired t test. ****$p < 0.0001$).

(G–I) Numbers of PAZs and DCVs in GH146-positive (G) and GH146-negative boutons (H). (I) Radar plots showing the number of GH146-positive boutons (black) and GH146-negative boutons (gray) in four clusters by PAZ and DCV number.

may be converted to each other; for example, unilobed boutons, with the least proportion, may be the intermediate state between complex boutons and simple boutons.

Distribution characteristics of PAZs in PN boutons

Most neurotransmitters are stored in clear core vesicles and are released into the synaptic cleft via PAZs (Torrealba and Carrasco 2004; Vaithianathan et al., 2016). In Drosophila, the majority of PAZs perform electron-dense ribbons under EM, called T-bar (Wichmann and Sigrist 2010; Butcher et al., 2012). Our study indicates that PAZ number is linearly correlated with the bouton volume, and PAZs are uniformly distributed in PN boutons with a constant density. Therefore, the size of boutons can estimate the quantity of PAZs. It is reported that PAZ density is constant in both neuromuscular junctions and the central nervous system in mice (Clarke et al., 2012). If all PAZs have an equal propensity to release neurotransmitters, the neurotransmission capacity of PN boutons should correspond to their volume; therefore, larger boutons have higher neurotransmission capacity. In *Drosophila*, prolonged deprivation of synaptic transmission from PNs leads to increased bouton size and PAZ density (Kremer et al., 2010; Pech et al., 2015). These two studies defined PAZ density by calculating the number of PAZs in individual boutons. However, we found that PN bouton sizes are variable, thus it is more precise to define the PAZ density by measuring the PAZ numbers within a certain volume. Here, we propose that PAZ number per square micron is the key determinant of the efficiency of boutons concerning information transmission, whereas PAZs per bouton determine the capability of information transmission. This hypothesis is based on the previous finding that positive correlation between quantal content per 100μm of terminal length and the amount of PAZs per 100 μm in neuromuscular junctions (Propst and Ko 1987) and the PAZ density remains relatively constant ($2.3/\mu m^2$) during synapse growth but impaired in aged mice (Clarke et al., 2012). In addition, the slopes of the linear fitting of PAZ number and bouton volume from our dataset and TEMCA2 dataset display no significant difference (Figure S3C). It suggests that the PAZ number per square micron in PN boutons is similar among individuals. Under disease conditions or in aged individuals, to maintain the transmission capacity, animals may compensate for reduced releasing capacity of synapse by increasing bouton size and PAZ number. It suggests the PAZ density decline can be a leading indicator of nervous system function degradation.

Characteristics of DCV distribution in PN boutons

In *Drosophila*, neuropeptides play key roles in the regulation of physiological and behavioral functions, including development, feeding, reproduction, and metabolism and neuromodulation roles in odor discrimination, locomotor control, and learning and memory (Nassel and Winther 2010; Riddiford et al. 2000; Kim and Rulifson 2004; Shen and Cai 2001; Isabel et al., 2005; Winther and Ignell 2010; Krashes et al., 2009; Nässel et al., 2008). Our study demonstrates that DCVs are enriched in GH146-positive PNs (Figure 4), reflecting the cell-specific distribution of DCVs. Recently, single-cell sequencing results revealed the subtype-specific expression of neuropeptide genes in GH146- positive PNs. AstA+ and DIP-eta are expressed in VA5 PNs, DIP-zeta is expressed in VA2 PNs, trol+ is expressed in VM2 PNs, danr is expressed in VA1 vPNs, and acj6 is expressed in D PNs (Croset et al., 2018; Xie et al., 2021). As neuropeptides can modulate structure and function of microcircuits (Nusbaum and Blitz 2012), specific PN subtypes releasing neuropeptides or not may play distinct roles in the establishment of sophisticated microcircuits that are responsible for olfactory cognition in calyx.

In neurons, neuropeptide is packaged into DCVs in the endoplasmic reticulum, transported to axons via the trans-Golgi network, and released at synaptic or extra-synaptic sites (Zupanc 1996). Therefore, DCV is the indicator of neural peptides. The spatial and temporal distribution pattern of DCV in the calyx microcircuits can provide the key evidence to analyze the function of peptides in the developmental and physiological processing of the cognition neural network. Our data, the TEMCA2 dataset, and the Hemibrain dataset (Bates et al., 2020; Scheffer et al., 2020; Li et al., 2020) are three samples to explore the footprints of neuropeptide-related DCV distribution in the olfactory cognition center. The three independent datasets establish a platform for cross comparing the general principles among individuals; for example, the quantitative measurement of the distribution of DCVs and PAZ density. The methods and tools developed in our work for dealing with the subcellular structure information in EM data automatically can help the further investigation on mechanisms through which intracellular components affect the connectome of the functional neural network, especially the DCV and neuropeptides responsible for microcircuits' plasticity.

Our volumetric reconstruction and quantitative analysis of PN neurites indicate that the intracellular distribution of DCVs display three patterns. Over 72% of DCVs are located adjacent to non-PAZ membranes. About 27% of DCVs are close to mitochondria. Only less than 1 percent is near to PAZ (Figures 3A and 3B). Therefore, our quantitative results suggest that the major release mode of DCV is in fusion with the membrane directly, instead of synaptic releasing from PAZ. Further physiology experiments are necessary to support this hypothesis. Some studies using *C. elegans* report that both DCV and mitochondria are transported to axons through the trans-Golgi network (Zupanc 1996; Roberts et al., 2016; Zhao et al. 2018). The DCVs locating to mitochondria may demonstrate the intermediate state of the transportation. In addition, the spatial correlation suggests a functional connection between DCV and mitochondria.

Limitations of the study

In the study, HRP-labeled EM was used to reconstruct target PN axonal boutons to reveal some new ultrastructural features concerning bouton shape, PAZ density, and DCV distribution. These ultrastructural features constitute new evidence or cues for characterizing and understanding the functional roles of PN subtypes in olfactory circuits. However, the current discovery originated from only one sample in a region of 20 μm × 20 μm × 25 μm, which approximately occupies $^1/_{30}$ of the main calyx of the MB. To assess whether the findings in the current study are general among individuals, further samples and studies are required. For instance, we may take advantage of published fly brain EM datasets, such as the TEMCA2 dataset and the Hemibrain dataset (Zheng et al., 2018; Scheffer et al., 2020). The study demonstrates that DCVs are preferentially distributed in GH146-positive boutons, which label about $^2/_3$ PNs; therefore, this conclusion is not specific enough to answer which PN subtypes contain the most DCVs. As all PNs are identified in TEMCA2 dataset and Hemibrain dataset (Zheng et al., 2018; Scheffer et al., 2020), annotation of DCVs in these two datasets should answer which specific PN subtypes contain the most DCVs.

STAR★METHODS

Detailed methods are provided in the online version of this paper and include the following:

- KEY RESOURCE TABLE
- RESOURCE AVAILABILITY
  - Lead contact
  - Materials availability
  - Data and code availability
- EXPERIMENTAL MODEL AND SUBJECT DETAILS
- METHOD DETAILS
  - EM sample preparation
  - EM data acquisition
  - Mitochondria detection
- QUANTIFICATION AND STATISTICAL ANALYSIS

SUPPLEMENTAL INFORMATION

Supplemental information can be found online at https://doi.org/10.1016/j.isci.2022.104180.

AUTHOR CONTRIBUTIONS

K. Y., A. G., Z. D., and K. Z. conceived the study and designed the experiment. K. Y. performed the EM sample preparation, volumetric reconstruction, PAZ and DCV annotation, data analysis, and wrote the original manuscript. T. L. proofread the reconstruction and annotation results and helped with the EM sample preparation and data analysis. H. H. and J. L. wrote the codes for the mitochondria detection and performed the

REFERENCES

Akaike, H. (1974). A new look at the statistical model identification. IEEE Trans. Automatic Con. *19*, 716–723.

Baltruschat, L., Prisco, L., Ranft, P., Lauritzen, J.S., Fiala, A., Bock, D.D., and Tavosanis, G. (2021). Circuit reorganization in the Drosophila mushroom body calyx accompanies memory consolidation. Cell Rep. *34*, 108871.

Barnstedt, O., Owald, D., Felsenberg, J., Brain, R., Moszynski, J.P., Talbot, C.B., Perrat, P.N., and Waddell, S. (2016). Memory-relevant mushroom body output synapses are cholinergic. Neuron *89*, 1237–1247.

Bates, A.S., Schlegel, P., Roberts, R.J.V., Drummond, N., Tamimi, I.F.M., Turnbull, R., Zhao, X., Marin, E.C., Popovici, P.D., Dhawan, S., et al. (2020). Complete connectomic reconstruction of olfactory projection neurons in the fly brain. Curr. Biol. *30*, 3183–3199.e6.

Butcher, N.J., Friedrich, A.B., Lu, Z., Tanimoto, H., and Meinertzhagen, I.A. (2012). Different classes of input and output neurons reveal new features in microglomeruli of the adult drosophila mushroom body calyx. J. Comp. Neurol. *520*, 2185–2201.

Butz, M., Worgotter, F., and van Ooyen, A. (2009). Activity-dependent structural plasticity. Brain Res. Rev. *60*, 287–305.

Clarke, G.L., Chen, J., and Nishimune, H. (2012). Presynaptic active zone density during development and synaptic plasticity. Front Mol. Neurosci. *5*, 12.

Croset, V., Treiber, C.D., and Waddell, S. (2018). Cellular diversity in the Drosophila midbrain revealed by single-cell transcriptomics. Elife *7*, e34550.

De Paola, V., Holtmaat, A., Knott, G., Song, S., Wilbrecht, L., Caroni, P., and Svoboda, K. (2006). Cell type-specific structural plasticity of axonal branches and boutons in the adult neocortex. Neuron *49*, 861–875.

Elkahlah, N.A., Rogow, J.A., Ahmed, M., and Clowney, E.J. (2020). Presynaptic developmental plasticity allows robust sparse wiring of the Drosophila mushroom body. Elife *9*, e52278.

Gondre-Lewis, M.C., Park, J.J., and Loh, Y.P. (2012). Cellular mechanisms for the biogenesis and transport of synaptic and dense-core vesicles. Int. Rev. Cell Mol. Biol. *299*, 27–115.

Gruntman, E., and Turner, G.C. (2013). Integration of the olfactory code across dendritic claws of single mushroom body neurons. Nat. Neurosci. *16*, 1821–1829.

Guo, A., Li, L., Xia, S.Z., Feng, C.H., Wolf, R., and Heisenberg, M. (1996). Conditioned visual flight orientation in Drosophila: dependence on age, practice, and diet. Learn. Mem. *3*, 49–59.

Heninger, G.R., Delgado, P.L., and Charney, D.S. (1996). The revised monoamine theory of depression: a modulatory role for monoamines, based on new findings from monoamine depletion experiments in humans. Pharmacopsychiatry *29*, 2–11.

Hökfelt, T., Barde, S., Xu, Z.D., Kuteeva, E., Rüegg, J., Le Maitre, E., Risling, M., Kehr, J., Ihnatko, R., Theodorsson, E., et al. (2018). Neuropeptide and small transmitter coexistence: fundamental studies and relevance to mental illness. Front. Neural Circuits. *12*, 106.

Hyman, S.E. (2005). Neurotransmitters. Curr. Biol. *15*, R154–R158.

Isabel, G., Martin, J.R., Chidami, S., Veenstra, J.A., and Rosay, P. (2005). AKH-producing neuroendocrine cell ablation decreases trehalose and induces behavioral changes in Drosophila. Am. J. Physiol. Regul. Integr. Comp. Physiol. *288*, R531–R538.

Jamann, N., Jordan, M., and Engelhardt, M. (2018). Activity-dependent axonal plasticity in sensory systems. Neuroscience *368*, 268–282.

Jia, Q., and Sieburth, D. (2021). Mitochondrial hydrogen peroxide positively regulates neuropeptide secretion during diet-induced activation of the oxidative stress response. Nat. Commun. *12*, 2304.

Jortner, R.A., Farivar, S.S., and Laurent, G. (2007). A simple connectivity scheme for sparse coding in an olfactory system. J. Neurosci. *27*, 1659–1669.

Kim, S.K., and Rulifson, E.J. (2004). Conserved mechanisms of glucose sensing and regulation by Drosophila corpora cardiaca cells. Nature *431*, 316–320.

Krashes, M.J., DasGupta, S., Vreede, A., White, B., Armstrong, J.D., and Waddell, S. (2009). A neural circuit mechanism integrating motivational state with memory expression in Drosophila. Cell *139*, 416–427.

Kremer, M.C., Christiansen, F., Leiss, F., Paehler, M., Knapek, S., Andlauer, T.F., Forstner, F., Kloppenburg, P., Sigrist, S.J., and Tavosanis, G. (2010). Structural long-term changes at mushroom body input synapses. Curr. Biol. *20*, 1938–1944.

Kuznetsov, I.A., and Kuznetsov, A.V. (2017). Chapter 13 - how dense core vesicles are delivered to axon terminals – a review of modeling approaches. In Modeling of Microscale Transport in Biological Processes, S.M. Becker, ed. (Academic Press), pp. 335–352.

Lai, S.L., Awasaki, T., Ito, K., and Lee, T. (2008). Clonal analysis of Drosophila antennal lobe neurons: diverse neuronal architectures in the lateral neuroblast lineage. Development *135*, 2883–2893.

Larsen, C.W., Hirst, E., Alexandre, C., and Vincent, J.-P. (2003). Segment boundary formation in Drosophila embryos. Development *130*, 5625–5635.

Lee, K., Zung, J., Li, P.H., Jain, V., and Seung, H.S. (2017). Superhuman accuracy on the SNEMI3D connectomics challenge. Preprint at arXiv. https://doi.org/10.48550/arXiv.1706.00120.

Leiss, F., Groh, C., Butcher, N.J., Meinertzhagen, I.A., and Tavosanis, G. (2009). Synaptic organization in the adult Drosophila mushroom body calyx. J. Comp. Neurol. *517*, 808–824.

Li, F., Lindsey, J.W., Marin, E.C., Otto, N., Dreher, M., Dempsey, G., Stark, I., Bates, A.S., Pleijzier, M.W., Schlegel, P., et al. (2020). The connectome of the adult Drosophila mushroom body provides insights into function. ELife *9*, e62576.

Li, H., Horns, F., Wu, B., Xie, Q., Li, J., Li, T., Luginbuhl, D.J., Quake, S.R., and Luo, L. (2017). Classifying Drosophila olfactory projection neuron subtypes by single-cell RNA sequencing. Cell *171*, 1206–1220.e22.

Li, H., Li, Y., Lei, Z., Wang, K., and Guo, A. (2013). Transformation of odor selectivity from projection neurons to single mushroom body neurons mapped with dual-color calcium imaging. Proc. Natl. Acad. Sci. U S A *110*, 12084–12089.

Liang, L., Li, Y., Potter, C.J., Yizhar, O., Deisseroth, K., Tsien, R.W., and Luo, L. (2013). GABAergic projection neurons route selective olfactory inputs to specific higher-order neurons. Neuron *79*, 917–931.

Lin, H.H., Lai, J.S., Chin, A.L., Chen, Y.C., and Chiang, A.S. (2007). A map of olfactory representation in the Drosophila mushroom body. Cell *128*, 1205–1217.

Lin, Z., Wei, D., Lichtman, J., and Pfister, H. (2021). PyTorch connectomics a scalable and flexible segmentation framework for EM connectomics. Preprint at arXiv. https://doi.org/10.48550/arXiv.2112.05754.

Liu, X., and Davis, R.L. (2009). The GABAergic anterior paired lateral neuron suppresses and is suppressed by olfactory learning. Nat. Neurosci. *12*, 53–59.

Mandal, A., Wong, H.C., Pinter, K., Mosqueda, N., Beirl, A., Lomash, R.M., Won, S., Kindt, K.S., and Drerup, C.M. (2021). Retrograde mitochondrial transport is essential for organelle distribution and health in zebrafish neurons. J. Neurosci. *41*, 1371–1392.

Mao, Z., and Davis, R.L. (2009). Eight different types of dopaminergic neurons innervate the Drosophila mushroom body neuropil: anatomical and physiological heterogeneity. Front Neural Circuits. *3*, 5.

Masse, N.Y., Turner, G.C., and Jefferis, G.S. (2009). Olfactory information processing in Drosophila. Curr. Biol. *19*, R700–R713.

Meinertzhagen, I.A. (1996). Ultrastructure and quantification of synapses in the insect nervous system. J. Neurosci. Methods. *69*, 59–73.

Nässel, D.R., Enell, L.E., Santos, J.G., Wegener, C., and Johard, H.A. (2008). A large population of diverse neurons in the Drosophila central nervous system expresses short neuropeptide F, suggesting multiple distributed peptide functions. BMC Neurosci. *9*, 90.

Nassel, D.R., and Winther, A.M. (2010). Drosophila neuropeptides in regulation of physiology and behavior. Prog. Neurobiol. *92*, 42–104.

Nusbaum, M.P., and Blitz, D.M. (2012). Neuropeptide modulation of microcircuits. Curr. Opin. Neurobiol. *22*, 592–601.

Nusbaum, M.P., Blitz, D.M., and Marder, E. (2017). Functional consequences of neuropeptide and small-molecule co-transmission. Nat. Rev. Neurosci. *18*, 389–403.

Pech, U., Revelo, N.H., Seitz, K.J., Rizzoli, S.O., and Fiala, A. (2015). Optical dissection of experience-dependent pre- and postsynaptic plasticity in the Drosophila brain. Cell Rep. *10*, 2083–2095.

Perez-Orive, J., Mazor, O., Turner, G.C., Cassenaer, S., Wilson, R.I., and Laurent, G. (2002). Oscillations and sparsening of odor representations in the mushroom body. Science *297*, 359–365.

Propst, J.W., and Ko, C.P. (1987). Correlations between active zone ultrastructure and synaptic function studied with freeze-fracture of physiologically identified neuromuscular junctions. J. Neurosci. *7*, 3654–3664.

Riddiford, L.M., Cherbas, P., and Truman, J.W. (2000). Ecdysone receptors and their biological actions. Vitam Horm. *60*, 1–73.

Roberts, R.F., Tang, M.Y., Fon, E.A., and Durcan, T.M. (2016). Defending the mitochondria: the pathways of mitophagy and mitochondrial-derived vesicles. Int. J. Biochem. Cell Biol. *79*, 427–436.

Root, C.M., Ko, K.I., Jafari, A., and Wang, J.W. (2011). Presynaptic facilitation by neuropeptide signaling mediates odor-driven food search. Cell *145*, 133–144.

Scheffer, L.K., Xu, C.S., Januszewski, M., Lu, Z., Takemura, S.-y., Hayworth, K.J., Huang, G.B., Shinomiya, K., Maitlin-Shepard, J., Berg, S., et al. (2020). A connectome and analysis of the adult Drosophila central brain. eLife *9*, e57443.

Schikorski, T., Young, S.M., Jr., and Hu, Y. (2007). Horseradish peroxidase cDNA as a marker for electron microscopy in neurons. J. Neurosci. Methods *165*, 210–215.

Schindelin, J., Arganda-Carreras, I., Frise, E., Kaynig, V., Longair, M., Pietzsch, T., Preibisch, S., Rueden, C., Saalfeld, S., Schmid, B., et al. (2012). Fiji: an open-source platform for biological-image analysis. Nat. Methods *9*, 676–682.

Schwarz, G. (1978). Estimating the dimension of a model. Ann. Stat. *6*, 461–464.

Shen, P., and Cai, H.N. (2001). Drosophila neuropeptide F mediates integration of chemosensory stimulation and conditioning of the nervous system by food. J. Neurobiol. *47*, 16–25.

Skaper, S.D. (2018). Neurotrophic factors: an overview. Methods Mol. Biol. *1727*, 1–17.

Stocker, R.F., Heimbeck, G., Gendre, N., and de Belle, J.S. (1997). Neuroblast ablation in

Drosophila P[GAL4] lines reveals origins of olfactory interneurons. J. Neurobiol. *32*, 443–456.

Torrealba, F., and Carrasco, M.A. (2004). A review on electron microscopy and neurotransmitter systems. Brain Res. Brain Res. Rev. *47*, 5–17.

Turner, G.C., Bazhenov, M., and Laurent, G. (2008). Olfactory representations by Drosophila mushroom body neurons. J. Neurophysiol. *99*, 734–746.

Vaithianathan, T., Henry, D., Akmentin, W., and Matthews, G. (2016). Nanoscale dynamics of synaptic vesicle trafficking and fusion at the presynaptic active zone. Elife *5*, e13245.

Van Bockstaele, E.J., Colago, E.E., and Valentino, R.J. (1996). Corticotropin-releasing factor-containing axon terminals synapse onto catecholamine dendrites and may presynaptically modulate other afferents in the rostral pole of the nucleus locus coeruleus in the rat brain. J. Comp. Neurol. *364*, 523–534.

Watts, R.J., Schuldiner, O., Perrino, J., Larsen, C., and Luo, L. (2004). Glia engulf degenerating axons during developmental axon pruning. Curr. Biol. *14*, 678–684.

Wichmann, C., and Sigrist, S.J. (2010). The active zone T-bar–a plasticity module? J. Neurogenet. *24*, 133–145.

Winther, A.M., and Ignell, R. (2010). Local peptidergic signaling in the antennal lobe shapes olfactory behavior. Fly (Austin) *4*, 167–171.

Xie, Q., Brbic, M., Horns, F., Kolluru, S.S., Jones, R.C., Li, J., Reddy, A.R., Xie, A., Kohani, S., Li, Z., et al. (2021). Temporal evolution of single-cell transcriptomes of Drosophila olfactory projection neurons. Elife *10*, e63450.

Yasuyama, K., Meinertzhagen, I.A., and Schurmann, F.W. (2002). Synaptic organization of the mushroom body calyx in Drosophila melanogaster. J. Comp. Neurol. *445*, 211–226.

Zhao, T., Hao, Y., and Kaplan, J.M. (2018). Axonal mitochondria modulate neuropeptide secretion through the hypoxic stress response in caenorhabditis elegans. Genetics *210*, 275–285.

Zheng, Z., Lauritzen, J.S., Perlman, E., Robinson, C.G., Nichols, M., Milkie, D., Torrens, O., Price, J., Fisher, C.B., Sharifi, N., et al. (2018). A complete electron microscopy volume of the brain of adult drosophila melanogaster. Cell *174*, 730–743.e22.

Zupanc, G.K. (1996). Peptidergic transmission: from morphological correlates to functional implications. Micron *27*, 35–91.

STAR★METHODS

KEY RESOURCE TABLE

REAGENT or RESOURCE	SOURCE	IDENTIFIER
Experimental models: Organisms/strains		
y[1] w[1118]; GH146-GAL4/CyO	(Stocker et al., 1997)	Bloomington Drosophila Stock Center: 30,026
UAS-CD2: HRP/CyO	(Larsen et al., 2003)	Bloomington Drosophila Stock Center: 8763
Critical commercial assays		
Glutaraldehyde Solution	SIGMA	CAT. NO. G5882
Osmium Tetroxide	TED PELLA	CAT. NO. 18451
Uranyl acetate	EMS	CAT. NO. 22400
SPI-Pon 812 Embeding Kit	SPI	CAT. NO. 2660
Software and algorithms		
TrakEM2	ImageJ	TrakEM2 (imagej.net)
SPSS Statistics 25	IBM	Downloading IBM SPSS Statistics 25

RESOURCE AVAILABILITY

Lead contact

Further Information and requests for EM sample preparation, volumetric reconstruction, and statistical analysis should be directed to and will be fulfilled by the lead contact, Ke Zhang (kezhang@bnu.edu.cn).

Materials availability

This study did not generate new unique regents.

Data and code availability

- The original EM dataset in the current study has not been deposited in a public repository but will be shared by the lead contact upon request.

- This paper does not report original code.

- Any additional information required to reanalyze the data reported in this paper is available from the lead contact upon request.

EXPERIMENTAL MODEL AND SUBJECT DETAILS

All strains were raised at 25 °C with a 12/12 h light/dark cycle in standard fly food (Guo et al., 1996). The y[1] w[1118]; GH146-GAL4/CyO strain ((Stocker et al., 1997), Bloomington Drosophila Stock Center: 30,026) was used to drive UAS-CD2:HRP/CyO ((Larsen et al., 2003), Bloomington Drosophila Stock Center: 8763).

METHOD DETAILS

EM sample preparation

EM sample preparation was performed as previously described(Watts et al., 2004), with the modifications described below. 4 brains from 4-day-old adult female *D. melanogaster* were dissected in 2.5% glutaraldehyde in 0.1 M phosphate buffer (PB; pH 7.4) on a cold plate at 4°C, then fixed in 2.5% glutaraldehyde overnight at 4°C. After three 10-min washes with 0.1 M Tris-HCl buffer (pH 7.4) at 4°C, brains were stained with 1 mg/mL DAB in 0.1 M Tris-HCl (pH 7.4) for 20 min at 4°C, then transferred to room temperature for 15 min. After three 10-min washes with 0.1 M PB, brains were fixed with 1% OsO4 in 0.1 M PB for 2 h at 4°C. After three 10-min washes with double-distilled water, brains were stained with 2% uranyl acetate overnight at 4°C. Dehydration and infiltration with resin were performed following standard protocols (Meinertzhagen 1996). Brains were dehydrated with 30% ethanol, 50% ethanol, 75% ethanol, 95% ethanol, 100% ethanol, 50% ethanol in acetone, 100% acetone step by step and each step was kept for 10 min at 4°C. Brains

were infiltrated with 30% resin (SPI-Pon 812 Embedding Kit, SPI) in acetone, 60% resin in acetone, pure resin step by step at room temperature and each step for 3 h. Then brains were polymerized at 60°C for 48 h.

EM data acquisition

One EM sample was trimmed and oriented vertically with the MB calyx on the top. Then the sample was coated with 10 nm gold and a layer of ~1.5 μm platinum was deposited on a surface perpendicular to the block face. Serial EM images were then acquired by focused ion beam scanning electron microscopy (FIB-SEM, Helios Nanolab 600i), which is controlled by Auto Slice & View software. The EM sample was imaged at 2 kV voltage and 0.34nA current in a aperture of 2.26 ✕ 10-5 μm diameter in x and y with 5-nm pixels and dwell time of 3 μs/pixel, in a small region of 20 ✕ 20 μm in the center of the MB calyx. A focused beam of 30-kV and 9.3nA gallium atoms was used to mill the EM sample every 40 nm to acquire a raw dataset of 658 slices. The 658 Serial EM images were merged into a stack and imported in to a TrakEM2 project in Fiji (Schindelin et al., 2012) and automatically enhanced the brightness and contrast. All reconstruction and annotation works are performed via the function of areatree, arealist and dissector in Fiji-TrakEM2 project. The skeleton length, segment number, volume, surface area, PAZ number, and DCV number were obtained by the built-in functions of the measurement of areatree, arealist, and dissector in Fiji-TrakEM2.

Mitochondria detection

To detect mitochondria from EM volume, we used a two-step method, including the binary segmentation step and connected components step. We first trained a 3D Residual U-Net to automatically segment mitochondria (Lee et al., 2017). To construct a mitochondrial ground truth dataset, 7 experienced annotators annotated all the mitochondria within an EM volume of 1024*1024*100 voxels. The dataset was then split into 6:2:2 for training, validation, and testing. Inspired by the thorough forms of data augmentation during affinity prediction (Lee et al., 2017), we also introduced misalignment (up to 16 pixels), missing sections (up to 2 slices) and out-of-focus section (up to 2 slices), except for the regular random rotations, flips and gray-scale transformations. After 25,000 training iterations, the trained network yielded 0.9042 precision and 0.8959 recall with respect of the pixel-wise segmentation on the test set. Then the network was applied to the full data with a blocking-scheme (block: 4096*4096*100, overlap: 128*128*4). After obtaining binary segmentations by thresholding the probability maps, we used connected components algorithm to obtain the unique ID of each 3D mitochondrion (Lin et al., 2021).

QUANTIFICATION AND STATISTICAL ANALYSIS

All statistical analyses were performed in IBM SPSS statistics 25. The Kolmogorov–Smirnov test was used to assess the normality of all data distributions. The unpaired t-test was used to compare two groups, and a one-way analysis of variance was used to compare more than two groups. Spearman's correlation coefficients were calculated for skeleton length and segment number, and Pearson's correlation coefficients were calculated for volume and DCV number, and PAZ number. Different models were used to obtain a high cluster quality, Akaike information criteria for morphology clustering, and Bayesian information criteria for PAZ-DCV clustering (Schwarz 1978; Akaike 1974).